

Conceptual design of a collimator for the neutron emission profile monitor in JT-60SA using Monte Carlo simulations

メタデータ	言語: eng 出版者: 公開日: 2021-12-17 キーワード (Ja): キーワード (En): 作成者: SUMIDA, Shuhei, Shinohara, K., Nishitani, Takeo, OGAWA, Kunihiro, Dando, T., Sukegawa, A.M., Ishikawa, M., Takada, Eiji, BIERWAGE, Andreas, Oyama, N. メールアドレス: 所属:
URL	http://hdl.handle.net/10655/00012769

This work is licensed under a Creative Commons Attribution 3.0 International License.



Conceptual Design of a Collimator for the Neutron Emission Profile Monitor in JT-60SA Using Monte-Carlo Simulations

S. Sumida^{1,a)}, K. Shinohara^{1,2}, T. Nishitani³, K. Ogawa^{3,4}, T. Bando¹, A. M. Sukegawa¹, M. Ishikawa¹, E. Takada⁵, A. Bierwage⁶ and N. Oyama¹

¹National Institutes for Quantum and Radiological Science and Technology, Naka, Ibaraki 311-0193, Japan

²The University of Tokyo, Kashiwa, Chiba 277-8561, Japan

³National Institute for Fusion Science, Toki, Gifu 509-5292, Japan

⁴The Graduate University for Advanced Studies, SOKENDAI, Toki, Gifu 509-5292, Japan

⁵National Institute of Technology, Toyama College, Toyama, Toyama 939-8630, Japan

⁶National Institutes for Quantum and Radiological Science and Technology, Rokkasho, Aomori 039-3212, Japan

(Presented XXXXX; received XXXXX; accepted XXXXX; published online XXXXX)

(Dates appearing here are provided by the Editorial Office)

Materials and structures of a collimator for a new neutron emission profile monitor in JT-60SA are examined through Monte-Carlo simulations using the MCNP code. First, the shielding properties of various material combinations are compared in order to determine a combination with high shielding performances against both neutrons and gamma-rays. It is found that a collimator consisting of borated polyethylene and lead has a high shielding performance against neutrons. Moreover, a high shielding performance against gamma-rays is obtained when a lead pipe with a radial thickness of 0.01 m is inserted into a collimation tube. Second, we demonstrate that it is possible to improve the spatial resolution to the desired level by installing a thin tubular extension structure that fits into the limited space available between the main collimator block and the tokamak device. Finally, the collimator structures that meet both the targeted spatial resolutions ($< 10\%$ of the plasma minor radius) and the targeted counting rate (10^5 cps order) are discussed.

I. INTRODUCTION

Neutron diagnostics is one of key tools for the study of energetic ion physics and for monitoring and controlling burning plasmas in fusion reactors. In particular, neutron emission profile measurements yield spatio-temporal information of the energetic ion distribution, ~~from which one can evaluate their~~ That information can be used to evaluate energetic ion confinement and transport. Therefore, neutron emission profile monitors are used in many fusion devices [1-4].

Deuterium (D) plasma experiments will be performed in the superconducting tokamak JT-60SA [5]. To obtain spatio-temporal information of the energetic ions, a neutron emission profile monitor is planned to be installed. Its multi-channel collimator is foreseen to be placed on a stage that is shared with other equipment, which limits the available space as well as allowed weight of the system. In general, a collimator having a high shielding performance, a high spatial resolution and a high time resolution is desirable. Given these targets and constraints, the main purpose of this study is to identify suitable materials and a suitable structural form for such a collimator.

~~Fast time response neutron scintillators will be adopted as detectors of the neutron emission profile monitor. The neutron detection part of the neutron emission profile~~

monitor is composed of a fast time-response neutron detector, a photomultiplier and a magnetic shield. Since the photomultiplier is affected by the magnetic field, a tubular magnetic shield similar to that adopted in LHD [6] will be used. A stilbene crystal scintillator is one of the candidates for the detector material [6,7-8]. ~~However,~~ Such scintillators are sensitive to not only neutrons, but also gamma-rays. Thus, the pulse-counting mode will be adopted for the detector in order to allow us to discriminate neutron signals from gamma-ray signals with a digital signal processing system. ~~However,~~ The gamma-rays can cause pileup events of signals and a gain shift in the photomultiplier tube. Therefore, the materials used for the collimator wall must have a high shielding performance against not only neutrons out of the sight line of the measurement, but also against gamma-rays.

In large-sized fusion devices, the main shielding materials that are often adopted for the collimators of neutron emission profile monitors are heavy concrete or high-density polyethylene. Both heavy concrete and polyethylene have high shielding performances against the neutrons. The hydrogen atoms contained in these materials play a central role for their neutron shielding performance. When polyethylene is adopted, lead blocks are often additionally used inside the collimator in order to attenuate the gamma-ray flux. This is because additional gamma-rays are generated inside the polyethylene block via neutron capture reactions that involve hydrogen atoms. In the case

^{a)}Electronic mail: sumida.shuhei@qst.go.jp

of heavy concrete, the material itself has a high gamma-ray shielding performance owing to it being doped with metals. In JET [1,2] and LHD [7,8-10], the collimators consist mainly of heavy concrete. Heavy concrete collimators are also planned to be installed in ITER [11-13]. On the other hand, a combination of the high-density polyethylene and the lead was adopted for JT-60U [6,7]. In this paper, the shielding performance of various combinations of these materials will be evaluated using Monte-Carlo neutron and gamma-ray transport simulations.

The targeted spatial resolution Δr and counting rate of the measurement system are $\Delta r < 0.1a$ and 10^5 cps order, respectively. Here, a is a plasma minor radius. For instance, to evaluate the energetic particle transport due to a sawtooth crash, a time resolution of < 100 ms is required. The high target counting rate on the order of 10^5 cps implies a time resolution up to 10 ms at a statistical error of $< \sim 3\%$ since the error is given by $1/\sqrt{n}$ where n is the number of counts. Note that too high a counting rate ~~is not desirable~~ **deteriorates the desired relation with the neutron flux, since** ~~for rates exceeding $\sim 10^6$ cps, counting losses occur due to pileup events, which reduce the accuracy of the measurement~~ [78]. A trade-off relation also exists between the counting rate and the spatial resolution. On the one hand, detailed spatial information of the energetic particles is desirable to evaluate their radial transport accurately and understand the physics of neutral beam current drive. On the other hand, the neutron flux coming into the detector decreases with increasing spatial resolution. Under this constraint, the targeted spatial resolution was chosen to be less than 10% of the minor radius; i.e., $\Delta r < 0.1a$. A collimator structure that achieves the target specifications under the given constraints is proposed in this paper on the basis of Monte-Carlo simulations.

This paper is organized as follows. In section II, the constraints limiting the size and weight of the neutron emission profile monitor system are laid out. In section III we describe the Monte-Carlo simulation model. Simulation results are presented and discussed in section IV, beginning with a comparison between several collimator material combinations with respect to their shielding performances against both neutrons and gamma-rays under the limited installation conditions. In addition, we evaluate the gamma-ray flux attenuation achieved with a lead pipe insertion into the collimation tube. So far, few works exist, where the shielding performance of the lead pipe insertion against the gamma-ray flux generated in the collimator is investigated using Monte-Carlo simulations. Next, we explore the idea of adding a thin tubular extension structure for the collimator and show that this allows to improve the spatial resolution in spite of limited installation space available. Finally, the spatial resolutions and the counting rates are estimated for various combinations of collimation lengths and inner diameters of a collimation tube, in order to determine the collimator structure that satisfies the targeted spatial resolution ($\Delta r < 0.1a$) and the targeted counting rate (10^5 cps order). We conclude with a summary in section V.

II. COLLIMATOR INSTALLATION CONDITIONS

Figure 1 shows schematic drawings of the available spaces for the collimator installation. A space with a size of $L 2 \text{ m} \times W 1.2 \text{ m} \times H 3 \text{ m}$ around $R = 10 \text{ m}$ and $Z = 0 \text{ m}$ is fully available and the main part of the collimator is planned to be installed in this space. Between that fully available space and the tokamak, there is some additional space that, however, is only partially available in order to avoid the interference with other equipment located just next to the collimator. The width of the partially available space is narrower than 1.2 m. Therefore, the collimator cannot be extended forward unless its width in that area is reduced below 1.2 m.

The maximum weight of the collimator permitted by the common stage on which it will be placed is 23 tons. In fact, the available space shown in Fig. 1 is the only place where such a heavy structure may be installed.

The collimator for JT-60SA must satisfy all of the above conditions.

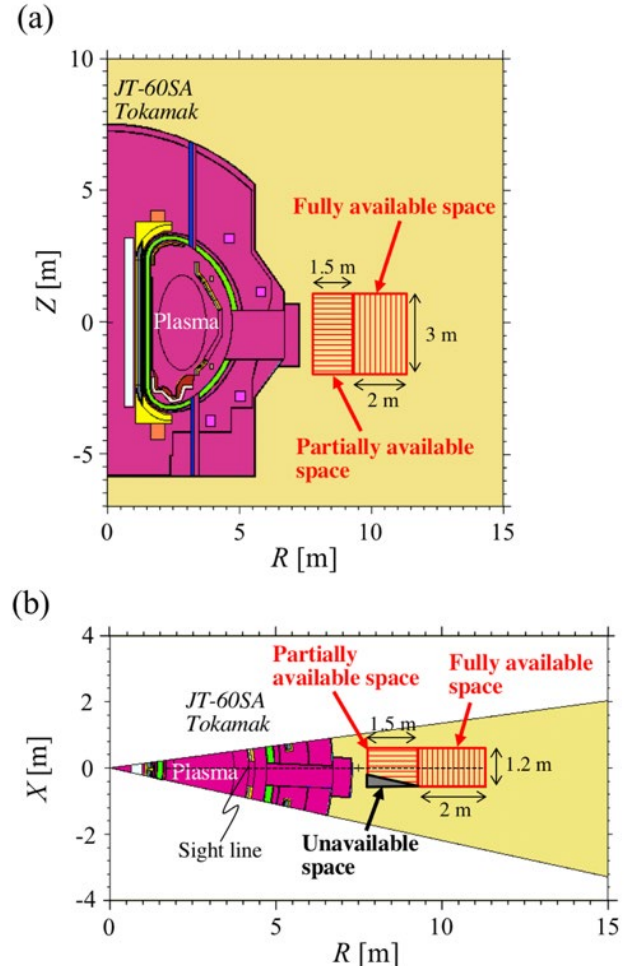


FIG. 1. (a) A schematic drawing of available spaces for the collimator installation. (b) A drawing of the spaces on the plane of $Z = 0 \text{ m}$. **Vertically and horizontally hatched areas are fully and partially available spaces, respectively.** The vertically hatched area indicates the fully available space. The partially available space is indicated by a horizontally hatched area.

whose unavailable portion is shaded gray in the top view (b). The drawings except for the available spaces are models for MCNP calculations (the details are described in section III).

III. MCNP CALCULATION MODEL

MCNP code (version 6.2) [14] is used for the Monte-Carlo simulations of neutron and gamma-ray transport. The cross-section library data for the MCNP calculations is given by FENDL (version 3.1) [15].

Figure 2 shows a schematic drawing of the model used for the MCNP calculation, which consists of a section of the JT-60SA tokamak and the collimator. The JT-60SA model consists of toroidal and poloidal superconducting magnetic field coils, stabilizing plates, a vacuum vessel, divertor structures, a cryostat and a plasma. In JT-60SA, there are 18

toroidal magnetic field coils, and the simulation volume encompasses a 20° wedge-shaped portion between two toroidal magnetic field coils, as shown in Fig. 2(eb). Reducing the simulated volume in this way allows to decrease the statistical errors made by the Monte-Carlo calculation with limited computational resources.

The neutron emission profile monitor in JT-60SA is meant to measure primarily neutrons originating from D-D fusion reactions. Although D-D fusion neutrons generated in the experiment have a certain spread in energy, the calculation assumes a source of neutrons with an energy of 2.45 MeV. These 2.45 MeV neutrons are assumed to be uniformly generated in a plasma modeled by a torus with an elliptic cross-section. In addition, the velocity vectors are taken to be isotropic. The lower bounds for the energies in the calculation are 10^{-11} MeV for the neutrons and 10^{-3} MeV for the gamma-rays. When the energy of a particle (neutron

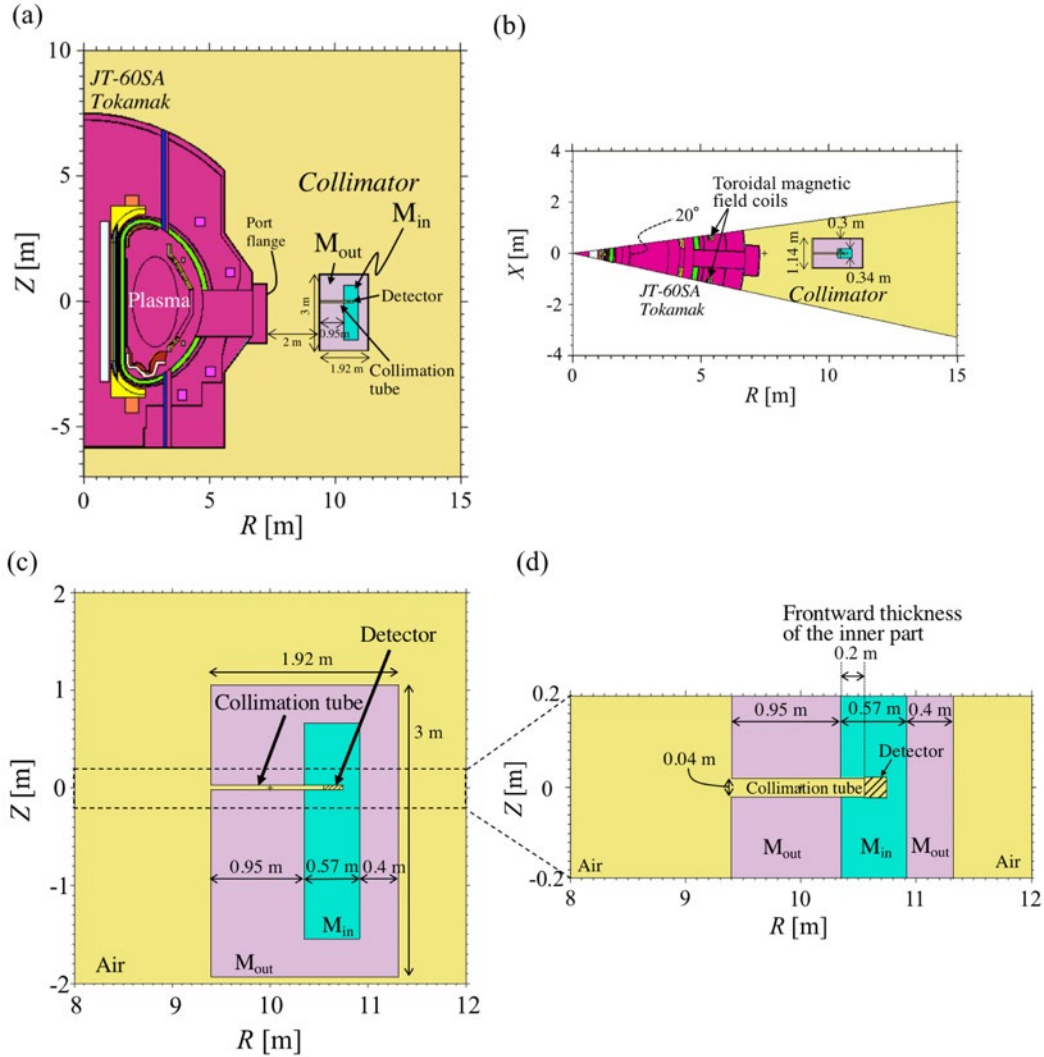


FIG. 2. (Panel (c) has been added.) (A size of a dashed quadrangle has been modified.) (The frontward thickness of the inner part is explicitly shown in panel (d)) (a) A schematic drawing of a MCNP calculation model for the JT-60SA tokamak and the collimator (a) viewed from the side on the R - Z plane and (b) viewed from top on the plane at $Z = 0$ m. Panel (c) shows an enlarged drawing of the entire collimator model and a further enlargement in panel (bd). An shows the structure and dimensions of the collimation tube in front of enlarged-drawing-of-the-model-around the detector and (c) a drawing of the model on the plane of $Z = 0$ m. Here, M_{out} and M_{in} stand for materials in outer and inner parts of the collimator, respectively. The outer part (M_{out}) fully encloses the inner part (M_{in}) except inside the collimation tube. Note that the actual system will have an array of collimation tubes (cf. Fig. 5), only one of which is shown here.

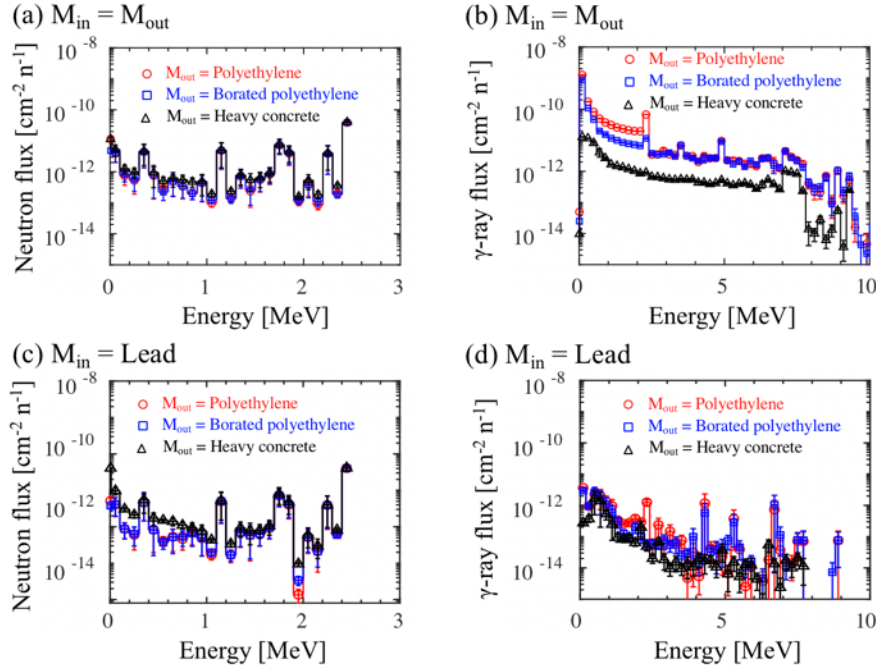


FIG. 3. Energy distributions of (a)(c) neutron fluxes and (b)(d) gamma-ray fluxes in the detector region. Circles, squares and triangles are fluxes in the cases of M_{out} = polyethylene, borated polyethylene and heavy concrete, respectively. Meanwhile, (a)(b) $M_{in} = M_{out}$ and (c)(d) $M_{in} = \text{lead}$.

or photon) drops below that limit, it is excluded from the transport calculation. Note that the neutron cutoff energy must be very low in order to take into account gamma-ray generation by the thermal neutrons.

The size of the collimator model is set to $L\ 1.92\ \text{m} \times W\ 1.14\ \text{m} \times H\ 3\ \text{m}$, which fits within the fully available space. In this model, the partially available space is not used. Only one detector and one collimation tube are present in the collimator model used to evaluate the respective shielding properties against stray neutrons and gamma-rays under JT-60SA environment conditions. In addition, the collimator model is split into an outer and an inner part in order to investigate how different combinations of various materials influence the shielding properties and to identify the appropriate (or optimal) material combination. As shown in the example in Fig. 2(bd), the frontward thicknesses of the outer and inner parts is 0.95 m and 0.2 m, respectively that of the inner part extending to the front plane of the detector region is 0.2 m. Here, the frontward thickness of the inner part is adopted from the design of the collimator in JT-60U [7]. The symbols M_{out} and M_{in} stand for the materials used for the outer and inner parts of the collimator, respectively. The following four materials are used for M_{out} and M_{in} : high-density polyethylene, 10%-borated high-density polyethylene, lead and heavy concrete. The compositions of the borated polyethylene and the heavy concrete used in this study are the same as in LHD [7,9,6,8,10,16], where these materials have shown high shielding performances. Thermal neutrons cause generations of gamma-rays via neutron capture reactions of $H(n,\gamma)D$ with hydrogen atoms contained in the collimator

TABLE I. Combinations of the collimator materials and their weights.

Outer material M_{out}	Inner material M_{in}	Weight of collimator [tons]
Polyethylene	Polyethylene	~6
Polyethylene	Lead	~11
Borated polyethylene	Borated polyethylene	~6
Borated polyethylene	Lead	~11
Heavy concrete	Heavy concrete	~23
Heavy concrete	Lead	~27

material. The boron of the borated polyethylene captures the thermal neutron via the reaction $^{10}\text{B}(n,\alpha)^7\text{Li}$ without gamma-ray generation. Colemanite ($\text{CaB}_3\text{O}_4(\text{OH})_3 \cdot \text{H}_2\text{O}$) and hematite (Fe_2O_3) doped in the heavy concrete also captures the thermal neutrons and attenuates the gamma-ray flux, respectively. Therefore, heavy concrete has higher shielding performances against neutrons and gamma-rays than normal concrete. While normal concrete is used as one of the collimator materials in TFTR [17,18], the higher shielding performance of heavy concrete motivated its choice for JT-60SA.

IV. SIMULATION RESULTS AND DISCUSSIONS

A. Investigation of material combination

Table I shows the combinations of collimator materials considered in this study. Three different materials are considered for the outer part and four materials (including lead for gamma-ray attenuation) for the inner part. For the sake of completeness and to systematically delineate trends, we also included the combination of heavy concrete and lead, although its weight exceeds the 23-ton weight limit of the stage.

Figure 3 shows the calculated energy distributions of the neutron and gamma-ray fluxes in the detector region. These energy distributions are histograms of the fluxes integrated over energy bins that are defined as follows. The first bin covers the range from the above-mentioned cutoff energy to 0.01 MeV. The range of the second bin is 0.01-0.1 MeV for neutrons and 0.01-0.2 MeV for gamma-rays. All other bin sizes are 0.1 MeV for neutrons and 0.2 MeV for gamma-rays. In the cases where the materials for both the outer and the inner parts are same, “ $M_{in} = M_{out}$ ”, the neutron energy distributions are similar to those in the cases when the material for the inner part is the lead, “ $M_{in} = \text{lead}$ ”. In contrast, the gamma-ray fluxes in the cases where “ $M_{in} = \text{lead}$ ” are much lower over a wide range of energies than in cases where “ $M_{in} = M_{out}$ ”. This is simply because “ $M_{in} = \text{lead}$ ” strongly attenuates both the background gamma-ray flux and the gamma-ray flux generated by the neutron capture reaction in the outer region of the collimator. Such a reduction of the gamma-ray flux coming into the detector region is important because gamma-rays can cause signal pileup events and shift the gain of the photomultiplier tube. For each of the 6 combinations of materials, Figure 4 shows (a) the respective fluxes of 2.45 MeV neutrons and (b) the total gamma-ray fluxes. Here, the value “2.45 MeV” represents the 2.4-2.5 MeV energy bin for the neutron flux, and the “total” gamma-ray flux is obtained by integration over all energy bins. One can see from Fig. 4 that the total gamma-ray fluxes in the cases where “ $M_{in} = M_{out}$ ” are much higher than in cases where “ $M_{in} = \text{lead}$ ”, while the 2.45 MeV neutron fluxes are nearly identical. Therefore, the choice “ $M_{in} = M_{out}$ ” is not an attractive option. The use of lead inside the collimator is desirable as it significantly attenuates the gamma-ray flux.

In JT-60SA, multiple collimator channels are envisioned, which will be aligned vertically as shown in Fig. 5. In order to properly measure the neutron emission profile, the cross-talk associated with scattered neutron fluxes from adjacent channels should be as low as possible. Figure 6 shows the calculated spatial distributions of the total neutron flux around the detector region for the configuration in Fig. 2. Here, the results for three outer materials and “ $M_{in} = \text{lead}$ ” are shown. The total neutron fluxes are obtained by integration over all energy bins. The neutron fluxes in the region $|Z| > 0.1$ m are less than 5% of the flux in the detector region in the cases where “ $M_{out} = \text{polyethylene or borated polyethylene}$ ”. In contrast, the neutron flux exceeds 10% everywhere in the case of “ $M_{out} = \text{heavy concrete}$ ”.

For a spatial resolution of $\Delta r < 0.1a$, the vertical distance between the detectors cannot be larger than 0.2 m

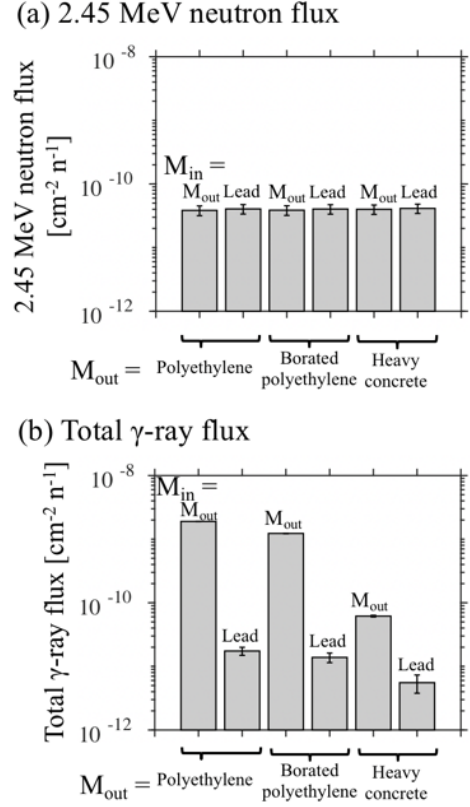


FIG. 4. (a) 2.45 MeV neutron fluxes and (b) total gamma-ray fluxes in the detector region. Here, the 2.45 MeV neutron flux is defined as a flux with energy from 2.4 to 2.5 MeV. From left to right, the material combinations are “ $M_{out} = M_{in} = \text{polyethylene}$ ”, “ $M_{out} = \text{polyethylene}$ and $M_{in} = \text{lead}$ ”, “ $M_{out} = M_{in} = \text{borated polyethylene}$ ”, “ $M_{out} = \text{borated polyethylene}$ and $M_{in} = \text{lead}$ ”, “ $M_{out} = M_{in} = \text{heavy concrete}$ ”, “ $M_{out} = \text{heavy concrete}$ and $M_{in} = \text{lead}$ ” in each figure.

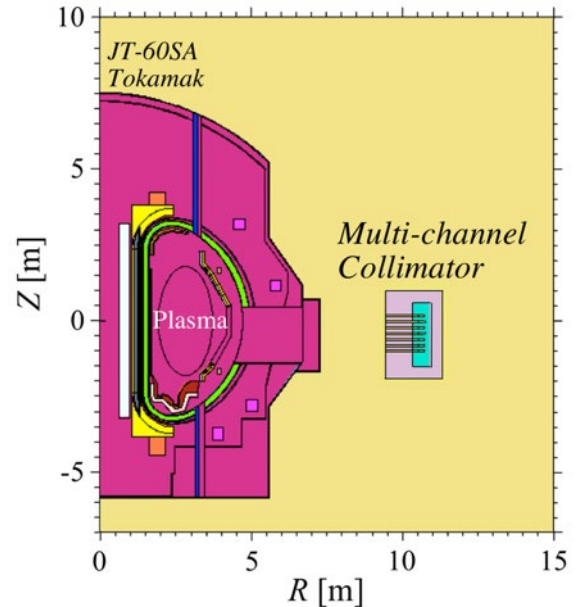


FIG. 5. A schematic drawing concept of a multi-channel collimator. The channels are planned to be aligned vertically. Note that this drawing does not show the final design, which is still being developed.

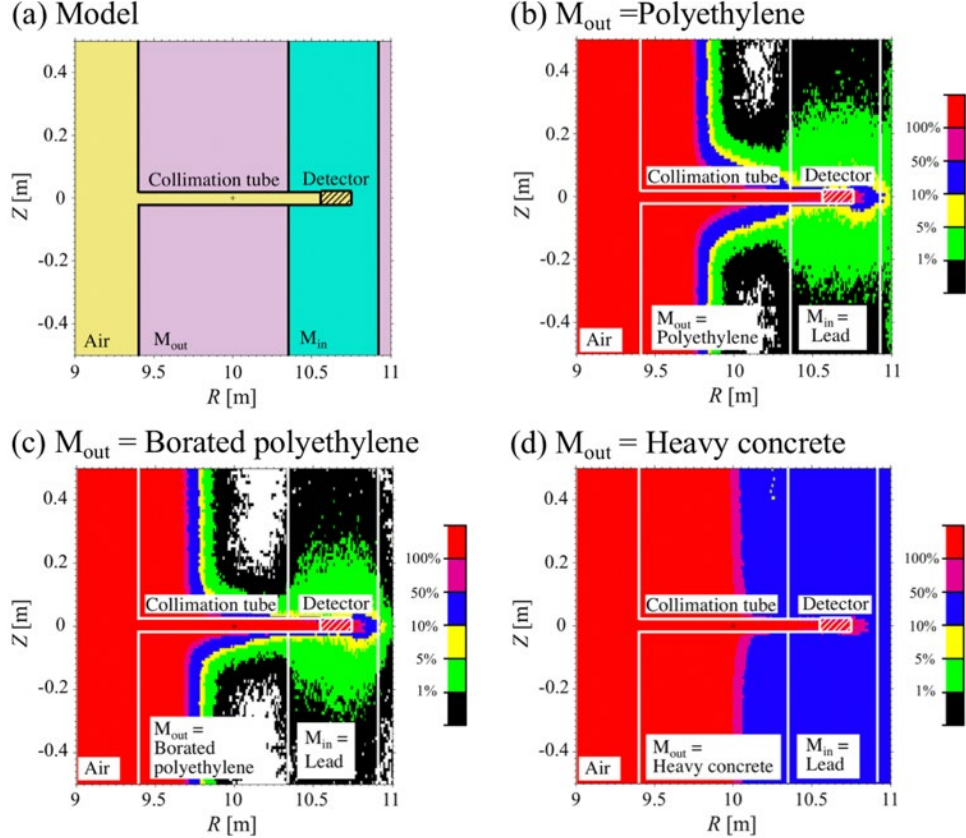


FIG. 6. (a) The model used for the calculations and (b)-(d) spatial distributions of the total neutron fluxes in the cases where “ $M_{in} = \text{lead}$ ”. The drawings shown here are enlarged around the detector as in Fig. 2(d). The shown distributions are ratios of fluxes to averaged ones in the detector region. Here, M_{out} is (b) polyethylene, (c) borated polyethylene and (d) heavy concrete.

because a in JT-60SA is 2 m in the vertical direction. For a detector spacing of 0.2 m, the cross-talks due to the scattered neutrons are expected to be relatively low for “ $M_{out} = \text{polyethylene or borated polyethylene}$ ”. In the case of “ $M_{out} = \text{heavy concrete and } M_{in} = \text{lead}$ ”, the high cross-talk is anticipated and the weight limit of the stage prohibits additional shielding. Therefore, a collimator consisting of “ $M_{out} = \text{heavy concrete and } M_{in} = \text{lead}$ ” is not suitable for the neutron emission profile monitor in JT-60SA.

Our results show clearly that polyethylene and borated polyethylene offer superior shielding performances against neutrons when compared to heavy concrete. The reason for this difference is thought to lie in the different densities of hydrogen atoms, which play a central role in neutron shielding. The hydrogen atom densities contained in borated polyethylene and polyethylene are >5 times higher than that in heavy concrete.

Meanwhile, we have seen in Fig. 4(b) that the gamma-ray flux in the case of “ $M_{out} = \text{borated polyethylene and } M_{in} = \text{lead}$ ” is slightly lower than that in the case of “ $M_{out} = \text{polyethylene and } M_{in} = \text{lead}$ ”. Therefore, in the following, we will focus on the scenario where the collimator consists of “ $M_{out} = \text{borated polyethylene and } M_{in} = \text{lead}$ ”. In this case, the total gamma-ray flux per source neutron is about $1.4 \times 10^{-11} \text{ cm}^{-2}\text{n}^{-1}$. Note that this is higher than $5.5 \times 10^{-12} \text{ cm}^{-2}\text{n}^{-1}$ in the case of “ $M_{out} = \text{heavy concrete and } M_{in} = \text{lead}$ ”, which

has the lowest gamma-ray flux among all combinations considered here. This difference is thought to be caused by the difference in the gamma-ray attenuation performance of the outer material M_{out} . Some gamma-rays generated in the region of M_{out} can pass through the collimation “hole” and reach the detector. Heavy concrete is able to attenuate these fluxes owing to it being doped hematite. However, a similar gamma-ray flux attenuation performance to “ $M_{out} = \text{heavy concrete}$ ” may be obtained in the case of “ $M_{out} = \text{polyethylene and } M_{in} = \text{lead}$ ” if a lead pipe is inserted into a collimation tube as shown in Fig. 7(b). This technique is expected to be effective even with relatively thin lead pipes because optical path lengths of the gamma-rays penetrating the lead pipe toward the detector are much longer than the pipe’s radial thickness Δr_{pipe} .

Figure 8 shows the Δr_{pipe} -dependence of the gamma-ray flux for lead pipes with fixed inner diameter 0.04 m (Fig. 7). One can see that, in the case of $\Delta r_{\text{pipe}} = 0.01 \text{ m}$, the gamma-ray flux is decreased to about one third of the flux without the lead pipe insertion. In this case, the total gamma-ray flux of $4.1 \times 10^{12} \text{ cm}^{-2}\text{n}^{-1}$ is lower than that in the case of “ $M_{out} = \text{heavy concrete and } M_{in} = \text{lead}$ ”, which had the least flux among all the cases in Fig. 4(b) without lead pipe insertion. Meanwhile, the neutron flux remains nearly unchanged. These results demonstrate that the collimator which consists of “ $M_{out} = \text{borated polyethylene and } M_{in} = \text{lead}$ ” has superior

shielding performances against both neutrons and gamma-rays when a lead pipe with a relatively small thickness of $\Delta r_{\text{pipe}} = 0.01$ m is inserted into the collimation tube. Hence, we will focus on this type of collimator in the following.

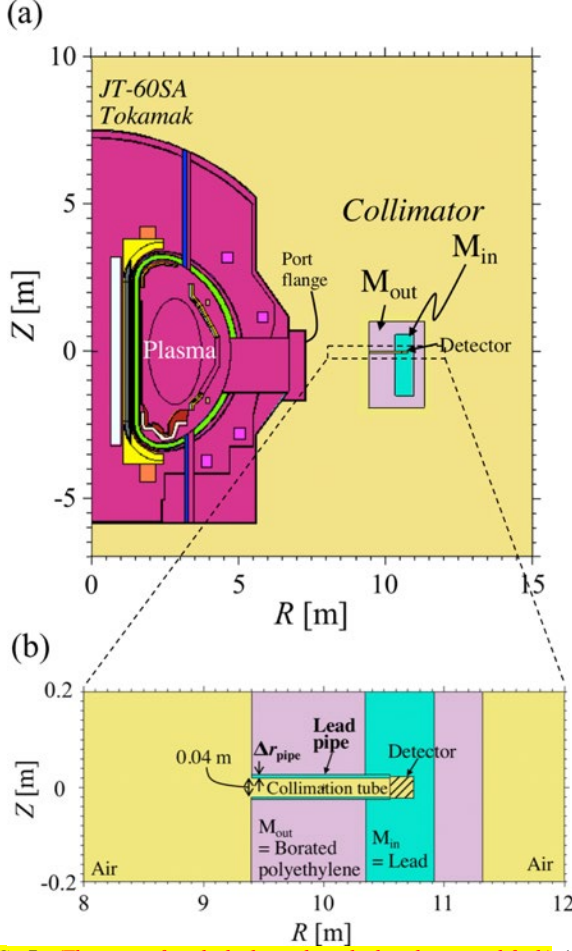


FIG. 7. (The size of a dashed quadrangle has been modified.) (a) A schematic drawing of the model in the case of the lead pipe insertion into the collimation tube and (b) its enlarged drawing around the detector. Here, Δr_{pipe} is a radial thickness of the lead pipe's wall.

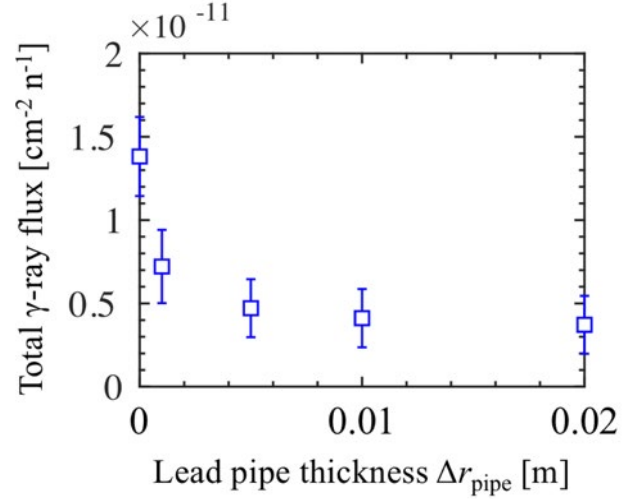


FIG. 8. Lead pipe thickness Δr_{pipe} dependence of the total gamma-ray flux in the detector region. Here, the flux at $\Delta r_{\text{pipe}} = 0$ m is the case without the lead pipe insertion.

B. Improvement of spatial resolution

A point-like source of 2.45 MeV neutrons ~~is~~ was scanned vertically at $R = 3$ m as shown in Fig. 9, and the flux profiles of 2.45 MeV neutrons at the detector ~~are~~ were calculated ~~in order~~ to evaluate the spatial resolution of the collimator. Here, the spatial resolution is defined to be twice the HWHM (Half Width at Half Maximum) of the 2.45 MeV neutron flux profile in the Z direction. For instance, when the HWHM of the profile is < 0.1 m, the spatial resolution Δr is < 0.2 m, or $\Delta r/a < 0.1$ for $a = 2$ m ~~vertically~~.

Figure 10 shows a schematic drawing of an “optical” collimator the wall of which stops the neutrons completely, without any scattering or penetration. The HWHM of this optical collimator can be estimated by,

$$\text{HWHM} = \frac{\Delta r}{2} = \frac{\phi d}{2l}, \quad (1)$$

where, l , d and ϕ are the collimation length, the distance from the detector and an inner diameter of the collimation tube, respectively. However, it is not obvious how accurately equation (1) approximates realistic conditions, where some neutrons ~~can reach the detector region after being are-scattered and/or penetrating the collimator wall, so that they can reach the detector region~~. Thus, we calculated the 2.45 MeV neutron flux profile using the MCNP code and compared the computed HWHM with that predicted by equation (1). The simulation was performed for the configuration in Fig. 7, which serves us as a reference case.

Figure 11 shows calculated results of the 2.45 MeV neutron flux profile in the reference case. Here, the flux profile is normalized by the mean value at $Z = 0$ m. One can see that the HWHM of the 2.45 MeV neutron flux profile in this reference case is about 0.12 m ($\Delta r/a \sim 0.12$), which is

rather close to the HWHM value of ~ 0.13 predicted by equation (1).

According to equation (1), there are two ways to improve the spatial resolution of the collimator when the detector position is fixed. One way is to reduce the inner diameter ϕ and the other is to increase the collimation length l . Under the optical collimator condition, the 2.45 MeV neutron flux into the detector region of the collimator is proportional to ϕ^4/l^2 [1]. Therefore, the 2.45 MeV neutron flux is expected to decrease more rapidly (4th power) with decreasing diameter ϕ than with a proportional increase of the length l (2nd power) when the spatial resolution is varied by an equal amount in each procedure.

We examined the following two cases. In the first case, the inner diameter ϕ is decreased from 0.04 m to 0.02 m. The value of ϕ^4/l^2 is reduced to $0.5^4 = 0.0625$ of that in the reference case. In the second case, the length l of the borated polyethylene region is extended 1 m forward as shown in Fig. 12. The value of ϕ^4/l^2 is $\sim 2^{-2} = \sim 0.25$ of that in the reference case. The spatial resolution in both cases is expected to be about a half of that of the reference case.

Figure 13 shows calculation results of the 2.45 MeV neutron flux profiles in the above two cases in comparison with the reference case. Here, the flux profiles are normalized by the respective mean values at $Z = 0$ m. The HWHMs are about 0.06 m, i.e. $\Delta r/a \sim 0.06$ in both cases, with the reduced diameter and with the extension part. These values are about a half of that in the reference case. Equation (1) gives a similar result.

Figure 14 shows the same results as Fig. 13, but without normalization. As expected, one can see that the absolute value of the 2.45 MeV neutron flux in the case with the reduced diameter is lower than in the other cases.

Note that, when the point-like neutron source is replaced by a torus-shaped plasma model with elliptic cross-section, the 2.45 MeV neutron fluxes to the detector in the cases with the reduced diameter and with the extension part are $\sim 2.5 \times 10^{-12} \text{ cm}^{-2}\text{n}^{-1}$ and $\sim 1.2 \times 10^{-11} \text{ cm}^{-2}\text{n}^{-1}$, respectively. These fluxes are ~ 0.06 and ~ 0.3 of that in the reference case. These values are consistent with the scaling ϕ^4/l^2 .

A lower flux of the 2.45 MeV neutrons results in a lower counting rate. To keep the counting rate high, it is necessary to minimize any further reduction of the neutron flux that may be caused by changes in ϕ and l . Thus, due to the scaling ϕ^4/l^2 , means that it is preferable to improve the spatial resolution by increasing the collimator length as in Fig. 12. Unfortunately, such an extension of the collimator structure with constant width cannot be installed in JT-60SA since it would interfere with other equipment in the partially available space (cf. Fig. 1).

A viable compromise is to extend only a narrow portion of the collimator around the collimation channel as shown in Fig. 15. This is expected to be effective because velocity vectors of the neutrons can be changed by scatterings in the thin extension part of the collimator. Consequently, most of the scattered neutrons moving towards the detector region will hit the collimator wall. As we have shown above, the collimator wall in the reference case has the high shielding

performance against the neutrons. As a result, most of the neutrons scattered in the thin extension part cannot reach the detector region. In the following, we consider a 1 m extension of the collimator length with reduced cross section $W 0.1 \text{ m} \times H 0.1 \text{ m}$ (as opposed to a bulk extension of size $W 1.14 \text{ m} \times H 3 \text{ m}$) as shown in Fig. 15. With this design, we avoid interference with other equipment, while expecting to achieve an improved spatial resolution of $\Delta r/a \sim 0.06$.

Figure 16 shows the calculated flux profiles of 2.45 MeV neutrons. Results are shown for two cases: (triangles) for the bulk extension as shown in Fig. 12 and (crosses) for the thin extension as shown in Fig. 15. In both cases, the 2.45 MeV neutron flux profiles are identical. This result demonstrates that the idea of the collimator with a thin extension part is an effective method for improving spatial resolution under the space limitations in JT-60SA.

To investigate how scattered low-energy neutrons affect the spatial resolution, we calculated profiles of the total neutron fluxes in the Z direction. Figure 17 shows the calculated profiles of the total neutron fluxes in the reference case, the reduced-diameter case and the extended case. The HWHM values here are almost the same as those of the 2.45 MeV neutron flux profiles shown in Fig. 13. In addition, Figure 18 shows the calculated total neutron flux profiles in the cases with the bulk extension (cf. Fig. 12) and with the thin extension (cf. Fig. 15). These profiles are identical. Therefore, the spatial resolutions are affected little by the scattered low-energy neutrons.

We also found that equation (1) yields results similar to the Monte-Carlo simulation, so that this approximate formula can be used to estimate the spatial resolution fairly accurately.

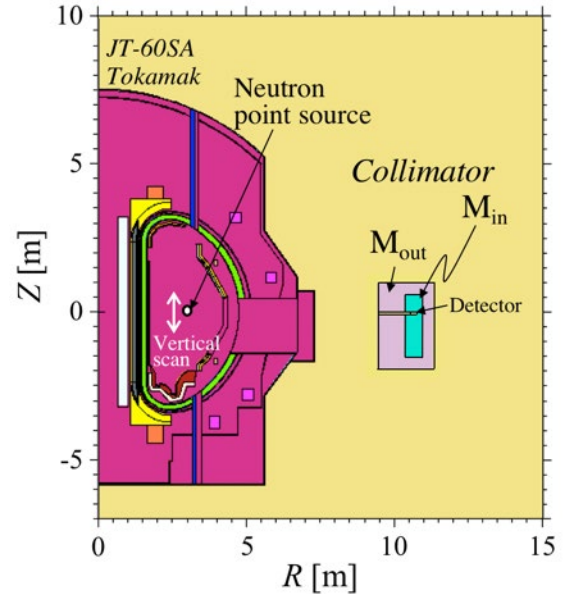


FIG. 9. (The text in this figure has been revised.) A schematic drawing of the model when a 2.45 MeV neutron point source is scanned vertically at $R = 3$ m to evaluate the neutron flux profile.

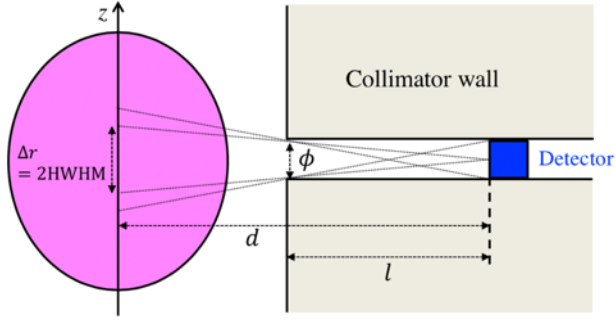


FIG. 10. A schematic drawing of the “optical” collimator. Here, l is a length of the collimation between the front planes of the collimator and of the detector. d is a distance from the front plane of the detector to an axis where the spatial resolution is evaluated. ϕ is an inner diameter of the collimation tube. Δr is the spatial resolution of this collimator.

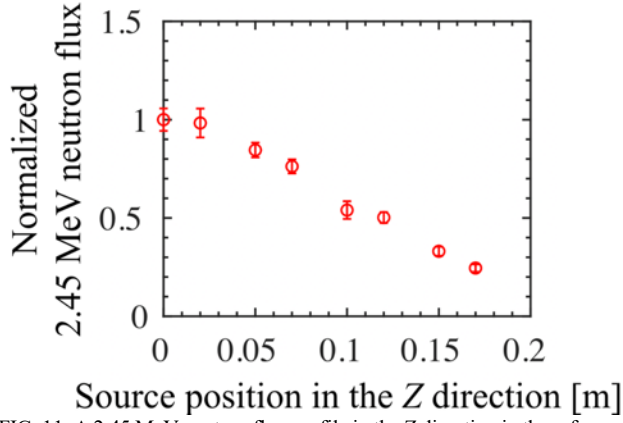


FIG. 11. A 2.45 MeV neutron flux profile in the Z direction in the reference case. The profile is normalized by an averaged flux at $Z = 0$ m.

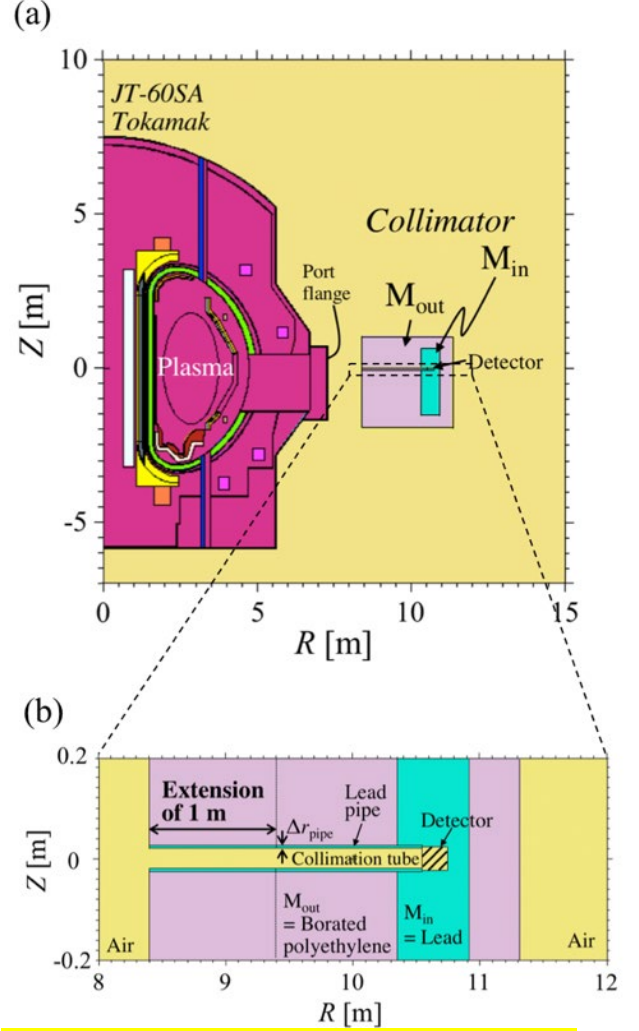


FIG. 12. (The size of a dashed quadrangle has been modified.) (a) A schematic drawing of the model in the extended collimator case and (b) its enlarged drawing around the detector.

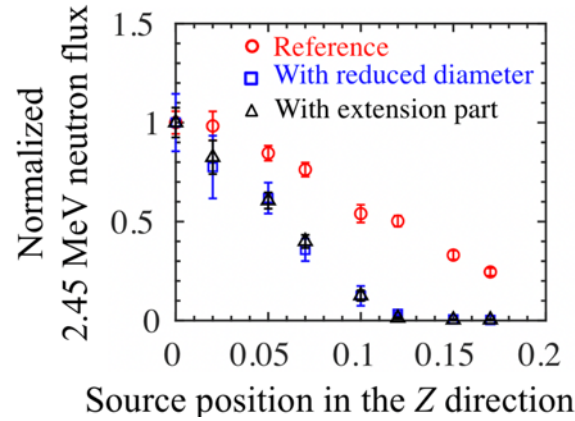


FIG. 13. 2.45 MeV neutron flux profiles in the Z direction. These profiles are normalized by the respective averaged fluxes at $Z = 0$ m. Circles, squares and triangles are the profiles in the reference case, the reduced-diameter case and the extended case, respectively.

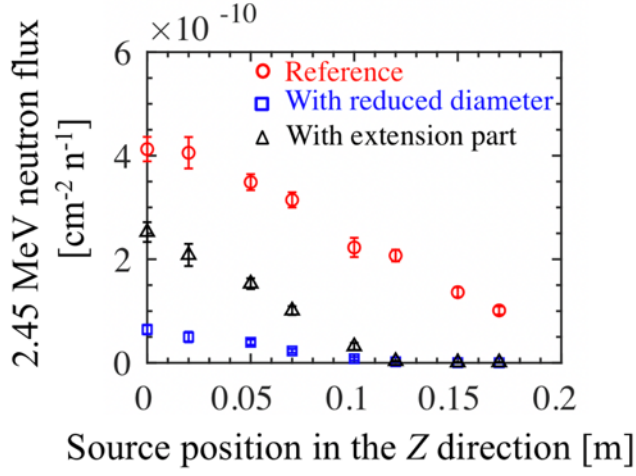


FIG. 14. 2.45 MeV neutron flux profiles in the Z direction without normalization. Circles, squares and triangles are profiles in the reference case, the reduced-diameter case and the extended case, respectively.

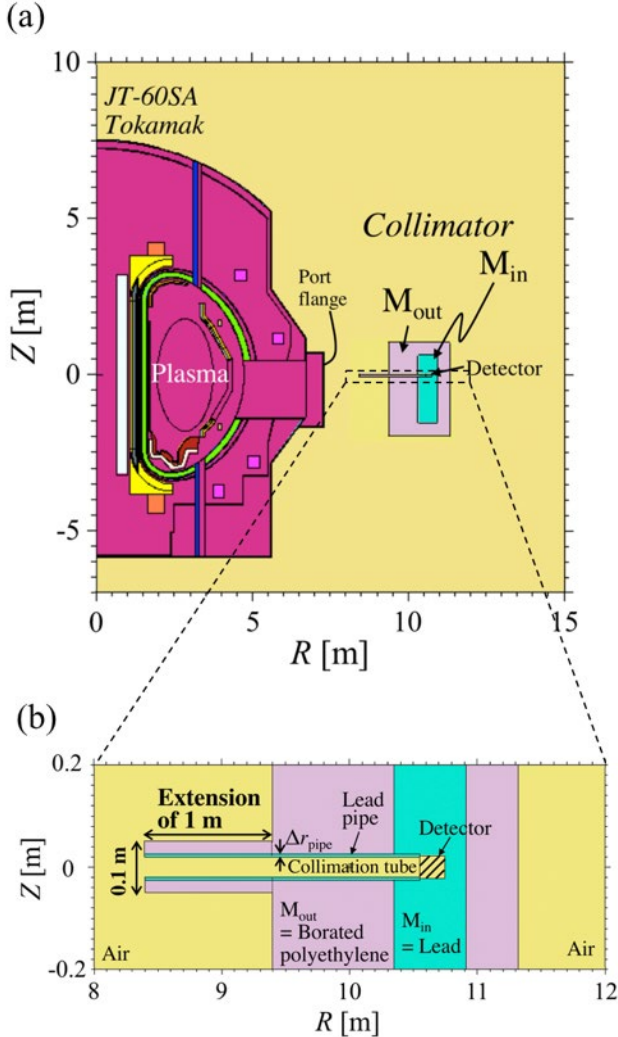


FIG. 15. (The size of a dashed quadrangle has been modified.) (a) A schematic drawing of the model in the case of the collimator with the thin tubular extension part and (b) its enlarged drawing around the detector. The cross section of the extension part is W 0.1 m × H 0.1 m.

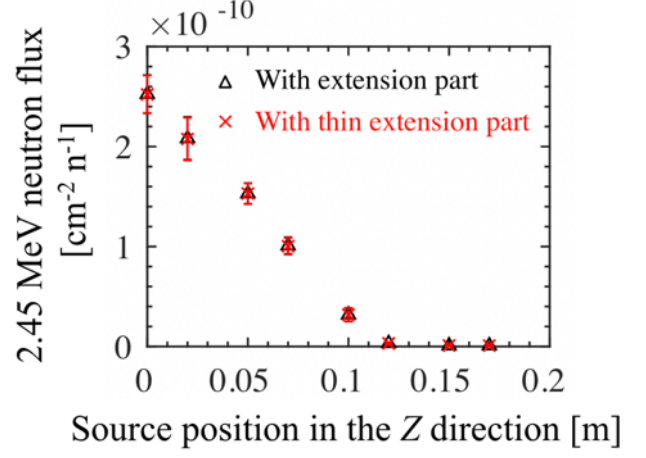


FIG. 16. 2.45 MeV neutron flux profiles in the Z direction. These profiles are normalized by the respective averaged fluxes at $Z=0$ m. Triangles and crosses are profiles in the cases of the collimators with the extension part shown in Fig. 12 and with the thin extension part shown in Fig. 15, respectively.

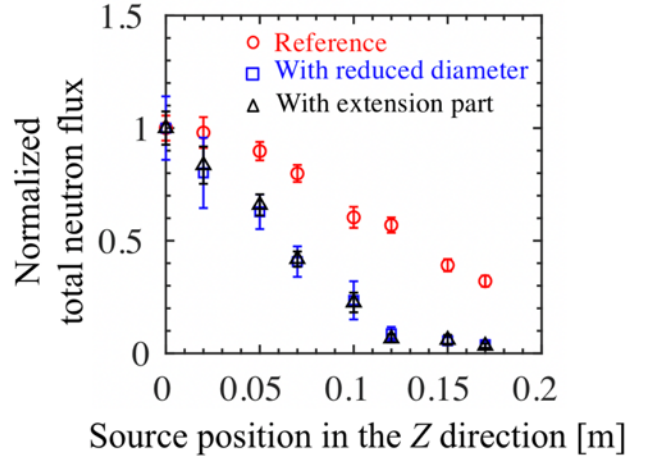


FIG. 17. Total neutron flux profiles in the Z direction. These profiles are normalized by the respective averaged fluxes at $Z=0$ m. Circles, squares and triangles represent, respectively, the profiles in the reference case, the reduced-diameter case and the extended case.

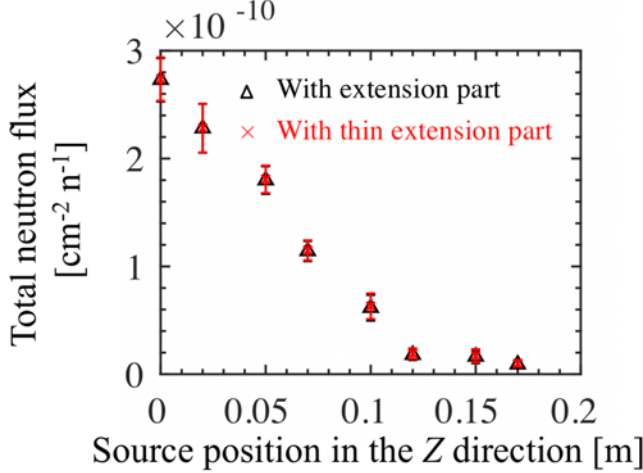


FIG. 18. Total neutron flux profiles in the Z direction. Triangles and crosses represent, respectively, profiles in the cases of the collimators with the extension part (shown in Fig. 12) and with the thin extension part (shown in Fig. 15), respectively.

C. Satisfaction of both target spatial resolution and target counting rate

In order to determine the regime of design parameters for which the envisioned collimator structure satisfies both the targeted spatial resolution ($\Delta r/a < 0.1$) and the targeted counting rate (10^5 cps order), we performed scans of the collimation length l and the inner diameters ϕ . Here, the spatial resolution is estimated using equation (1), and the counting rate is estimated from the numerically computed neutron flux in the detector region.

The absolute value for the detection efficiency of the detector is required for the estimation of the counting rate. In a previous study performed for LHD [9,10], the absolute detection efficiency of the stilbene detector was evaluated by calculating its pulse height response function with the PHTIS code [19]. The same method employing the PHTIS code (version 3.20) is used in the present work.

In order to calculate the pulse height response function, PHITS requires the energy distribution of the neutron flux to the detector, which was obtained here with the MCNP code. Figure 4719 shows the energy distribution of the neutron flux computed by MCNP in the reference case. Figure 4820 shows the resulting pulse height response function computed by PHITS. Here, the size of the stilbene scintillator is taken to be 30 mm in diameter and 10 mm in thickness. From this response function, the absolute detection efficiency was evaluated to be ~ 0.51 counts/(n/cm²) when a threshold energy is 0.1 MeV_{ee} (electron-equivalent energy).

The maximal neutron emission rate S_n in JT-60SA is estimated to be on the order of 10^{17} n/s [5]. The “typical” value in most experiments can be assumed to be significantly lower than that. Here, we choose $S_n = 5 \times 10^{15}$ n/s to utilize this system in various experiments. In high power experiments, where S_n is much higher than 5×10^{15} n/s and the counting rate would exceed $\sim 10^6$ cps for the default

configuration, we can adjust the counting rate to the desired level of 10^5 cps order by reducing the inner diameter ϕ of the collimation tube. For our nominal neutron emission rate $S_n = 5 \times 10^{15}$ n/s and the evaluated detection efficiency, the counting rate in the reference case is estimated to be $\sim 2.2 \times 10^5$ cps.

Assuming that the counting rate is proportional to the neutron flux, one can use this computed absolute value of the counting rate in the reference case to estimate the counting rates for different collimator parameters via the scaling ϕ^4/l^2 . Figure 4921 shows the results of this extrapolation for the counting rate (dashed lines) for a range of values of the extension length l_{ext} and inner diameter ϕ . The corresponding spatial resolution estimated with equation (1) is also shown (solid lines). In the case without the extension structure ($l_{\text{ext}} = 0$), the target spatial resolution ($\Delta r/a < 0.1$) and the target counting rate (10^5 cps order) cannot be satisfied simultaneously. Achieving both targets becomes possible only by adding an extension structure with length $l_{\text{ext}} > 0.1$ m (shaded area). Therefore, a thin extension structure as in Fig. 15 is an essential component of our collimator design.

As mentioned above, our simulation model assumes a uniform neutron emission profile for the entire plasma volume. In a real plasma, the emission rate varies across the plasma radius. This and the fact that each channel of the neutron emission profile monitor is located at a different position imply that the counting rates in an actual experiment will differ significantly from channel to channel. In order to ensure that each detector receives the desired counting rate on the order of 10^5 cps, it is important to choose suitably tailored values of ϕ and l for each channel. The optimization of these collimator design parameters for realistic neutron emission profiles will be the subject of a future study.

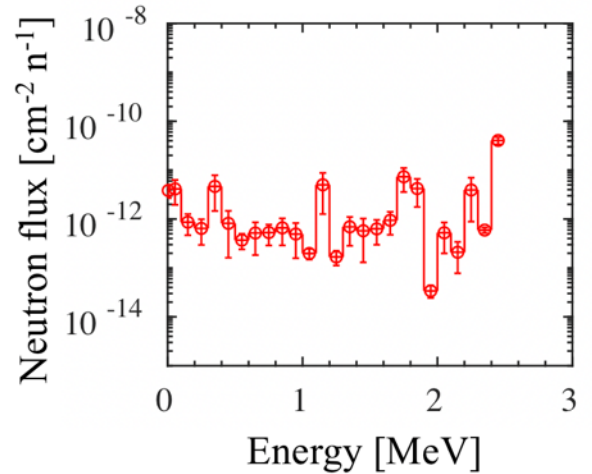


FIG. 4719. Energy distribution of the neutron flux to the detector region in the reference case. This distribution is used for the calculation of the pulse height response function of the stilbene detector with the PHITS code.

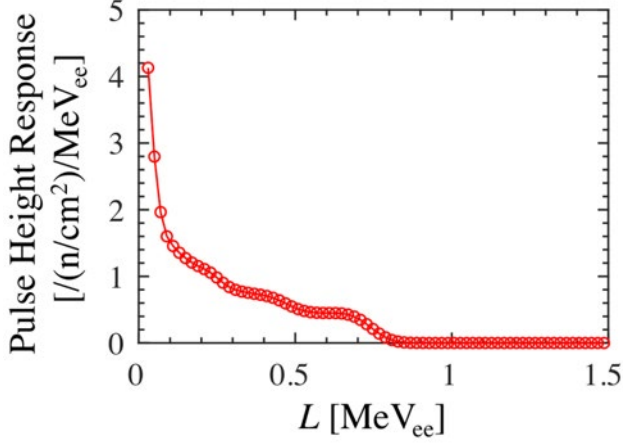


FIG. 1820. The calculated pulse height response function of the stilbene detector. Here, L is a light output energy and MeV_{ee} is a unit of electron-equivalent energy. L can be estimated by $L = 0.203 E_{\text{proton}}^{1.424}$ in the case of the stilbene detector adopted in LHD [910], where E_{proton} is the deposited energy by recoiled protons.

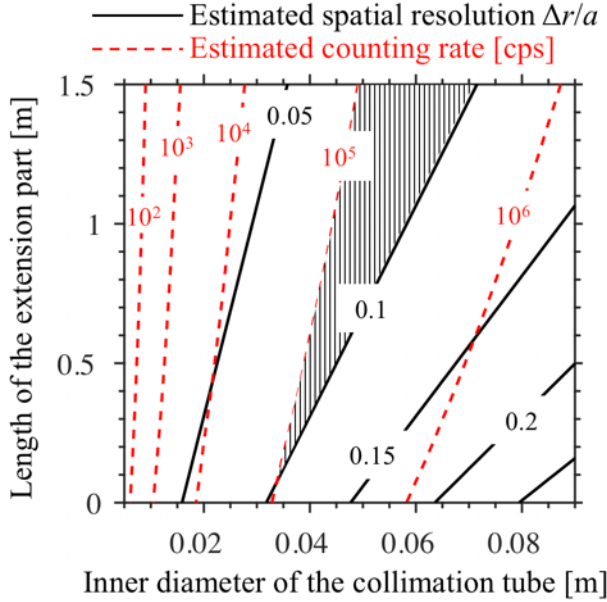


FIG. 1921. Spatial resolutions $\Delta r/a$ (solid lines) and counting rates of the detector (dashed lines) estimated by using equation (1) and the neutron flux scaling ϕ^4/l^2 , respectively. Here, the neutron emission rate is 5×10^{15} n/s. The counting rate is extrapolated from the estimation in the reference case. A hatched area indicates the parameter regime where both the targeted spatial resolution ($\Delta r/a < 0.1$) and the targeted counting rate (10^5 cps order) are satisfied.

V. SUMMARY

In this study, materials and structures of the collimator for the new neutron emission profile monitor in JT-60SA have been examined using numerical simulations with the Monte-Carlo code MCNP. In order to determine the collimator material combination with the highest shielding

performances against both neutrons and gamma-rays, several combinations of the following materials were considered: polyethylene, borated polyethylene, lead and heavy concrete. The highest shielding performance against neutrons was obtained by combining borated polyethylene and lead for the outer and inner parts of the collimator, respectively; i.e., “ M_{out} = borated polyethylene and M_{in} = lead”. In addition, it was demonstrated that inserting a thin lead pipe into the collimation tube is effective for the shielding the detector from gamma-ray fluxes that are generated in the borated polyethylene region. When the radial thickness of the lead pipe is 0.01 m, the collimator consisting of “ M_{out} = borated polyethylene and M_{in} = lead” has the highest shielding performances against both neutrons and gamma-rays among all material combinations shown in Table I.

In order to improve spatial resolution, the increment of the collimator length is preferable to the reduction of the inner diameter since the reduction amount of the counting rate is smaller. However, to achieve the targeted spatial resolution ($\Delta r/a < 0.1$), the collimator length has to be increased towards the tokamak device beyond the limit of the fully available space. Spatial constraints prohibit a bulk extension of the collimator with cross-section W 1.14 m \times H 3 m because of the interference with other equipment. Thus, we examined the idea of adding the thin tubular extension structure with cross-section W 0.1 m \times H 0.1 m in order to improve the spatial resolution under the limited installation conditions. The results show that the targeted spatial resolution can be achieved by the extension of the thin structure.

Finally, the spatial resolution and the counting rate at the neutron emission rate $S_n = 5 \times 10^{15}$ n/s were estimated for a range of values of the collimation length l and the inner diameter ϕ of the collimation tube. The results indicate that both the targeted spatial resolution ($\Delta r/a < 0.1$) and the targeted counting rate (10^5 cps order) can be satisfied when the collimator has the thin extension structure with a length of 0.1 m or more. Therefore, we conclude that a collimator that consists of “ M_{out} = borated polyethylene and M_{in} = lead”, and which is equipped with a lead pipe insertion (with $\Delta r_{\text{pipe}} = 0.01$ m) and with a thin extension structure is suitable for the neutron emission profile monitor in JT-60SA.

In this study, we assumed that the neutron source is uniform in the plasma region. In the future, we are planning to consider neutron source profiles based on realistic plasma profiles, which will be required for detailed designs of the collimator structures, such as the inner diameter and the length of each collimation channel, as well as the cross section of the extension part. In addition, the sizes of the outer and inner parts of the collimator will be optimized for the final detailed designs. The influence of scattered neutrons and gamma-rays coming from the nearby equipment on a signal-to-background ratio will be also investigated, although we expect that this will affect the fluxes only be a negligibly small amount.

ACKNOWLEDGMENTS

This work was partially supported by the NINS program of Promoting Research by Networking among Institutions (Grant Number 01411702) and conducted in the QST tokamak plasma collaborative research program which was started in 2019.

DATA AVAILABILITY

The data that support the findings of this study are available from the corresponding author upon reasonable request.

- ¹J. M. Adams, O. N. Jarvis, G. J. Sadler, D. B. Syme and N. Watkins, Nucl. Instrum. Methods Phys. Res. A **329**, 277 (1993).
- ²O. N. Jarvis, J. M. Adams, F. B. Marcus and G. J. Sadler, Fusion Eng. and Des. **34-35**, 59 (1997).
- ³M. Ishikawa *et al.*, Nucl. Fusion **45**, 1474 (2005).
- ⁴K. Ogawa, M. Isobe, T. Nishitani, S. Murakami, R. Seki, H. Nuga, S. Kamio, Y. Fujiwara, H. Yamaguchi, Y. Saito, S. Maeta, M. Osakabe and LHD Experiment Group, Nucl. Fusion **59**, 076017 (2019).
- ⁵JT-60SA Research Plan, http://www.jt60sa.org/pdfs/JT-60SA_Res_Plan.pdf, (cited August, 2020).
- ¹⁰K. Ogawa, M. Isobe, T. Nishitani and T. Kobuchi, Rev. Sci. Instrum. **89**, 113509 (2018).
- ⁶K. Ogawa, M. Isobe, T. Nishitani and T. Kobuchi, Rev. Sci. Instrum. **89**, 113509 (2018).
- ⁶M. Ishikawa, T. Nishitani, A. Morioka, M. Takechi, K. Shinohara, M. Shimada, Y. Miura, M. Nagami and Yu. A. Kaschuck, Rev. Sci. Instrum. **73**, 4237 (2002).
- ⁸K. Ogawa, M. Isobe, E. Takada, Y. Uchida, K. Ochiai, H. Tomita, A. Uritani, T. Kobuchi and Y. Takeiri, Rev. Sci. Instrum. **85**, 11E110 (2014).
- ⁸M. Isobe *et al.*, Rev. Sci. Instrum. **81**, 10D310 (2010).
- ⁹T. Nishitani, K. Ogawa and M. Isobe, Fusion Eng. Des. **123**, 1020 (2017).
- ¹⁰K. Ogawa, M. Isobe, T. Nishitani and T. Kobuchi, Rev. Sci. Instrum. **89**, 113509 (2018).
- ¹¹A. V. Krasilnikov *et al.*, Nucl. Fusion **45**, 1503 (2005).
- ¹²D. Marocco, B. Esposito and F. Moro, J. Instrum. **7**, C03033 (2012).
- ¹³D. Marocco, F. Moro, B. Esposito, G. Brolatti, R. Villari, S. Salasca and B. Cantone, Fusion Eng. Des. **88**, 1371 (2013).
- ¹⁴C.J. Werner *et al.*, *MCNP Version 6.2 Release Notes, LA-UR-18-20808* (Los Alamos National Laboratory, Los Alamos, 2018).
- ¹⁵FENDL-3.1, <https://www-nds.iaea.org/fendl/>, (cited August, 2020).
- ¹⁶T. Nishitani, T. Ozaki, K. Saito, S. Kamio, K. Ogawa, M. Isobe and M. Osakabe, Plasma Fus. Res. **14**, 3405048 (2019).
- ¹⁷A. L. Roquemore, R. C. Chouinard, M. Diesso, R. Palladino, J. D. Strachan and G. D. Tait, Rev. Sci. Instrum. **61**, 3163 (1990).
- ¹⁸A. L. Roquemore, M. Bitter, L. C. Johnson and S. von Goeier, Rev. Sci. Instrum. **68**, 544 (1997).
- ¹⁹T. Sato *et al.*, J. Nucl. Sci. Technol. **55(5-6)**, 684 (2018).